European Congress on Computational Methods in Applied Sciences and Engineering
ECCOMAS 2004
P. Neittaanmäki, T. Rossi, K. Majava, and O. Pironneau (eds.)
W. Rodi and P. Le Quéré (assoc. eds.)
Jyväskylä, 24–28 July 2004

DISCONTINUITY-CAPTURING DIRECTIONAL DISSIPATION (DCDD) IN COMPUTATION OF TURBULENT FLOWS

Franco Rispoli*, Pierpaolo Borrelli‡, and Tayfun E. Tezduyar†

* Dipartimento di Meccanica e Aeronautica
Universita degli Studi di Roma "La Sapienza", Via Eudossiana, 18, I-00184 Roma, Italy
e-mail: rispoli@dma.ing.uniroma1.it

‡ SINTEF Energy Research AS
Kolbjorn Hejes Vei 1A, 7465 Trondheim, Norway
e-mail: pierpaolo.borrelli@sintef.no

† Mechanical Engineering, Rice University – MS 321
6100 Main Street, Houston, TX 77005, USA
e-mail: tezduyar@rice.edu

Key words: Stabilized formulations, SUPG and PSPG stabilizations, DCDD stabilization, Stabilization parameters, Advective and diffusive length scales.

Abstract. *Stabilized formulations are now widely used in the computation of turbulent flows. The Streamline-Upwind/Petrov-Galerkin (SUPG) and Pressure-Stabilizing/Petrov-Galerkin (PSPG) methods are among the most popular stabilized formulations. The Discontinuity Capturing Directional Dissipation (DCDD) was first introduced as a complement to the SUPG and PSPG stabilizations for the computation of incompressible flows in the presence of sharp solution gradients. The DCDD stabilization takes effect where there is a sharp gradient in the velocity field and introduces dissipation in the direction of that gradient. The length scale used in defining the DCDD stabilization is based on the solution gradient. Here we describe how the DCDD stabilization, in combination with the SUPG and PSPG stabilizations, can be applied to computation of turbulent flows. We examine the similarity between the DCDD stabilization and a purely dissipative energy cascade model. To evaluate the performance of the DCDD stabilization, we compute as test problems a plane channel flow and an axial flow fan rotor.*

1 INTRODUCTION

Considerable progress has been made in recent decades in development of computational fluid mechanics tools capable of predicting flow patterns and aerodynamic performance in real-world applications. Many computational challenges involved in simulation and modeling of complex flow problems have been addressed with a number of advanced numerical methods, including Large Eddy Simulation (LES) turbulence modeling and stabilized formulations. Several LES techniques, with different modeling strategies, have been proposed for finite element computation of flow problems (see [1] for an introductory review). Among them are the nonlinear Galerkin methods [2], variational multiscale methods [3, 4, 5], and techniques based on the dynamic Smagorinsky model (see, for example, [6]).

Most of the computational fluid mechanics techniques reported in the literature in the past two decades are based on stabilized formulations. In finite element computation of flow problems, the Streamline-Upwind/Petrov-Galerkin (SUPG) formulation for incompressible flows [7, 8], the SUPG formulation for compressible flows [9, 10, 11], and the Pressure-Stabilizing/Petrov-Galerkin (PSPG) formulation for incompressible flows [12] are some of the most prevalent stabilized methods. Stabilized formulations such as the SUPG and PSPG formulations have a number of well-known advantages. They prevent numerical instabilities in solving problems with high Reynolds or Mach numbers and shocks or thin boundary layers, as well as when using equal-order interpolation functions for velocity and pressure. They also substantially improve the convergence rate in iterative solution of the large, coupled nonlinear equation system that needs to be solved at every time step of a flow computation. The SUPG and PSPG formulations are among the stabilized methods that achieve these objectives without introducing excessive numerical dissipation.

The stabilized formulation introduced in [13] for advection–diffusion–reaction equations included a shock-capturing (discontinuity-capturing) term, and accounted for the interaction between the discontinuity-capturing and SUPG terms. The formulation precluded augmentation of the SUPG effect by the discontinuity-capturing effect when the advection and discontinuity directions coincide. The PSPG formulation for the Navier–Stokes equations of incompressible flows, introduced in [12], assures numerical stability while allowing us to use equal-order interpolation functions for velocity and pressure. An earlier version of this stabilized formulation for Stokes flow was introduced in [14].

A stabilization parameter, which is almost always known as "τ", is embedded in the SUPG and PSPG formulations. It involves a measure of the local length scale (also known as "element length") and other parameters such as the element Reynolds and Courant numbers. Judicious selection of the stabilization parameter plays an important role in determining the accuracy of the formulation. Various element lengths and τs were proposed starting with those in [7, 8] and [9, 10, 11], followed by the one introduced in [13], and those proposed in the subsequently reported SUPG and PSPG methods.

Recently, new ways of computing the τs were introduced in [15, 16, 17, 18, 19, 20, 21, 22, 23] in the context of the advection-diffusion equation and the Navier–Stokes equations of incompressible flows. To be used in conjunction with the SUPG/PSPG formulation of incompressible flows, a Discontinuity-Capturing Directional Dissipation (DCDD) stabilization was introduced in [16, 17, 18] for computation of flow fields with sharp gradients. This involved a second element length scale, which was also also introduced in [16, 17, 18] and is based on the solution gradient. This new element length scale is used together with the element length scales already defined (directly or indirectly) in [13] and [15]. Recognizing this second element length as a diffusion length scale, new stabilization parameters for the diffusive limit were introduced in [17, 18, 19, 20, 21, 22, 23].

The DCDD stabilization takes effect where there is a sharp gradient in the velocity field and introduces dissipation in the direction of that gradient. The way the DCDD stabilization is added to the finite element formulation precludes augmentation of the SUPG effect by the DCDD effect when the advection and discontinuity directions coincide. In this paper, we apply the DCDD stabilization to computation of turbulent flows. With respect to the traditional use of upwind schemes [24, 25] for advective terms or explicit frequency low-pass filter [26], the DCDD introduces a dissipative term that is based on discontinuity filtering. With respect to the standard LES model, we see that the DCDD and the Smagorinsky subgrid viscosities are correlated in space. Here, we apply the DCDD stabilization specifically to computation of turbulent flows in complex wall-bounded flow configurations. In these computations, we use a parallel multi-level method [27]. The parallel solution algorithm includes an overlapping domain decomposition technique based on an inexact explicit nonlinear Schwarz method introduced in [28].

The governing equations are given in Section 2. We summarize the SUPG and PSPG formulations in Section 3, and describe the calculation of the stabilization parameters in Section 4. The DCDD stabilization is described in Section 5. The parameters of the LES model are given in Section 6. The test computations are reported in Section 7, and the concluding remarks are given in Section 8.

2 GOVERNING EQUATIONS

Let $\Omega \subset \mathbb{R}^{n_{sd}}$ be the spatial domain with boundary Γ, and $(0,T)$ be the time domain. The Navier–Stokes equations of incompressible flows can be written on Ω and $\forall t \in (0,T)$ as

$$\rho\left(\frac{\partial \mathbf{u}}{\partial t} + \mathbf{u}\cdot\boldsymbol{\nabla}\mathbf{u} - \mathbf{f}\right) - \boldsymbol{\nabla}\cdot\boldsymbol{\sigma} = 0, \tag{1}$$

$$\boldsymbol{\nabla}\cdot\mathbf{u} = 0, \tag{2}$$

where ρ, $\mathbf{u}$ and $\mathbf{f}$ are the density, velocity and the external force, respectively. The stress tensor $\boldsymbol{\sigma}$ is defined as

$$\boldsymbol{\sigma}(p,\mathbf{u}) = -p\mathbf{I} + 2\mu\boldsymbol{\varepsilon}(\mathbf{u}). \tag{3}$$

Here p is the pressure, $\mathbf{I}$ is the identity tensor, $\mu = \rho\nu$ is the viscosity, ν is the kinematic viscosity, and $\boldsymbol{\varepsilon}(\mathbf{u})$ is the strain-rate tensor:

$$\boldsymbol{\varepsilon}(\mathbf{u}) = \frac{1}{2}\left((\boldsymbol{\nabla}\mathbf{u}) + (\boldsymbol{\nabla}\mathbf{u})^T\right). \tag{4}$$

The essential and natural boundary conditions for Eq. (1) are represented as

$$\mathbf{u} = \mathbf{g} \text{ on } \Gamma_{\mathrm{g}}, \qquad \mathbf{n}\cdot\boldsymbol{\sigma} = \mathbf{h} \text{ on } \Gamma_{\mathrm{h}}, \tag{5}$$

where Γ_g and Γ_h are complementary subsets of the boundary Γ, $\mathbf{n}$ is the unit normal vector, and $\mathbf{g}$ and $\mathbf{h}$ are given functions. A divergence-free velocity field $\mathbf{u}_0(\mathbf{x})$ is specified as the initial condition.

3 SUPG/PSPG STABILIZATIONS

Given Eqs. (1)–(2), we form some suitably-defined finite-dimensional trial solution and test function spaces for velocity and pressure: $\mathcal{S}^h_{\mathbf{u}}$, $\mathcal{V}^h_{\mathbf{u}}$, $\mathcal{S}^h_p$ and $\mathcal{V}^h_p = \mathcal{S}^h_p$. The stabilized finite element formulation of Eqs. (1)–(2) can be written as follows: find $\mathbf{u}^h \in \mathcal{S}^h_{\mathbf{u}}$ and $p^h \in \mathcal{S}^h_p$ such that $\forall \mathbf{w}^h \in \mathcal{V}^h_{\mathbf{u}}$ and $\forall q^h \in \mathcal{V}^h_p$:

$$\begin{aligned}
&\int_\Omega \mathbf{w}^h \cdot \rho\left(\frac{\partial \mathbf{u}^h}{\partial t} + \mathbf{u}^h\cdot\boldsymbol{\nabla}\mathbf{u}^h - \mathbf{f}^h\right) d\Omega + \int_\Omega \boldsymbol{\varepsilon}(\mathbf{w}^h) : \boldsymbol{\sigma}(p^h, \mathbf{u}^h) d\Omega - \int_{\Gamma_{\mathrm{h}}} \mathbf{w}^h\cdot\mathbf{h}^h d\Gamma \\
+ &\int_\Omega q^h \boldsymbol{\nabla}\cdot\mathbf{u}^h d\Omega + \sum_{e=1}^{n_{el}} \int_{\Omega^e} \frac{1}{\rho}\left[\tau_{\mathrm{SUPG}}\rho\mathbf{u}^h\cdot\nabla\mathbf{w}^h + \tau_{\mathrm{PSPG}}\nabla q^h\right]\cdot\left[Ł(p^h,\mathbf{u}^h) - \rho\mathbf{f}^h\right] d\Omega \\
+ &\sum_{e=1}^{n_{el}} \int_{\Omega^e} \nu_{\mathrm{LSIC}}\boldsymbol{\nabla}\cdot\mathbf{w}^h\rho\boldsymbol{\nabla}\cdot\mathbf{u}^h d\Omega \;=\; 0,
\end{aligned} \tag{6}$$

where

$$Ł(q^h, \mathbf{w}^h) = \rho\left(\frac{\partial \mathbf{w}^h}{\partial t} + \mathbf{u}^h\cdot\boldsymbol{\nabla}\mathbf{w}^h\right) - \boldsymbol{\nabla}\cdot\boldsymbol{\sigma}(q^h, \mathbf{w}^h). \tag{7}$$

Here τ_{SUPG}, τ_{PSPG} and ν_{LSIC} are the SUPG, PSPG and LSIC (least-squares on incompressibility constraint) stabilization parameters.

4 CALCULATION OF THE UGN/RGN-BASED STABILIZATION PARAMETERS

Various ways of calculating the stabilization parameters for incompressible flows were covered earlier in detail in [15, 16, 17, 18, 19, 20, 21, 22, 23]. In this section we focus on the versions of the stabilization parameters (τs) denoted by the subscript UGN, namely

the UGN/RGN-based stabilization parameters. For this purpose, we first define the unit vectors $\mathbf{s}$ and $\mathbf{r}$:

$$\mathbf{s} = \frac{\mathbf{u}^h}{\|\mathbf{u}^h\|} , \tag{8}$$

$$\mathbf{r} = \frac{\boldsymbol{\nabla}\|\mathbf{u}^h\|}{\| \boldsymbol{\nabla}\|\mathbf{u}^h\| \|} . \tag{9}$$

The components of $(\tau_{\text{SUPG}})_{\text{UGN}}$ corresponding to the advection-, transient- and diffusion-dominated limits were defined in [18, 19, 20, 21, 22, 23] as follows:

$$\tau_{\text{SUGN1}} = \left(\sum_{a=1}^{n_{en}} |\mathbf{u}^h \cdot \boldsymbol{\nabla} N_a| \right)^{-1} , \tag{10}$$

$$\tau_{\text{SUGN2}} = \frac{\Delta t}{2}, \tag{11}$$

$$\tau_{\text{SUGN3}} = \frac{h_{\text{RGN}}^2}{4\nu} , \tag{12}$$

where n_{en} is the number of element nodes and N_a is the interpolation function associated with node a, and the "element length" h_{RGN} is defined as

$$h_{\text{RGN}} = 2 \left(\sum_{a=1}^{n_{en}} |\mathbf{r} \cdot \boldsymbol{\nabla} N_a| \right)^{-1} . \tag{13}$$

Based on Eq. (10), the "element length" h_{UGN} is defined as

$$h_{\text{UGN}} = 2\|\mathbf{u}^h\| \ \tau_{\text{SUGN1}} . \tag{14}$$

Although writing a direct expression for τ_{SUGN1} as given by Eq. (10) was pointed out in [18, 19, 20, 21, 22, 23], the element length definition one obtains by combining Eq. (10) and Eq. (14) was first introduced (as a direct expression for h_{UGN}) in [13]. The expression for h_{RGN} as given by Eq. (13) was first introduced in [16, 17, 18]. It was noted in [18, 19, 20, 21, 22, 23] that h_{UGN} and h_{RGN} can be viewed as the local length scales corresponding to the advection- and diffusion-dominated limits, respectively.

We now define $(\tau_{\text{SUPG}})_{\text{UGN}}$, $(\tau_{\text{PSPG}})_{\text{UGN}}$, and $(\nu_{\text{LSIC}})_{\text{UGN}}$ as follows:

$$(\tau_{\text{SUPG}})_{\text{UGN}} = \left(\frac{1}{\tau_{\text{SUGN1}}^r} + \frac{1}{\tau_{\text{SUGN2}}^r} + \frac{1}{\tau_{\text{SUGN3}}^r} \right)^{-\frac{1}{r}} , \tag{15}$$

$$(\tau_{\text{PSPG}})_{\text{UGN}} = (\tau_{\text{SUPG}})_{\text{UGN}}, \tag{16}$$

$$(\nu_{\text{LSIC}})_{\text{UGN}} = (\tau_{\text{SUPG}})_{\text{UGN}} \ \|\mathbf{u}^h\|^2 . \tag{17}$$

Eq. (15) is based on the inverse of $(\tau_{\text{SUPG}})_{\text{UGN}}$ being defined as the r-norm of the vector with components $\frac{1}{\tau_{\text{SUGN1}}}$, $\frac{1}{\tau_{\text{SUGN2}}}$ and $\frac{1}{\tau_{\text{SUGN3}}}$. We note that the higher the integer r is, the

sharper the switching between τ_{SUGN1}, τ_{SUGN2} and τ_{SUGN3} becomes. This "*r-switch*" was introduced in [15]. Typically, $r = 2$. The expressions for τ_{SUGN3} and $(\nu_{\text{LSIC}})_{\text{UGN}}$, given respectively by Eqs. (12) and (17), were proposed in [18, 19, 20, 21, 22, 23]. The "SUPG viscosity" ν_{SUPG} is defined as

$$\nu_{\text{SUPG}} = \tau_{\text{SUPG}} \|\mathbf{u}^h\|^2. \tag{18}$$

The space–time versions of τ_{SUGN1}, τ_{SUGN2}, τ_{SUGN3}, $(\tau_{\text{SUPG}})_{\text{UGN}}$, $(\tau_{\text{PSPG}})_{\text{UGN}}$, and $(\nu_{\text{LSIC}})_{\text{UGN}}$, given respectively by Eqs. (10), (11), (12), (15), (16), and (17), were defined in [18, 19, 20, 21, 22, 23].

5 DISCONTINUITY-CAPTURING DIRECTIONAL DISSIPATION (DCDD)

As an alternative to the LSIC stabilization, the Discontinuity-Capturing Directional Dissipation (DCDD) stabilization was proposed in [16, 17, 18]. In describing the DCDD stabilization, we first define the "DCDD viscosity" ν_{DCDD} and the DCDD stabilization parameter τ_{DCDD}:

$$\nu_{\text{DCDD}} = \tau_{\text{DCDD}} \|\mathbf{u}^h\|^2, \tag{19}$$

$$\tau_{\text{DCDD}} = \frac{h_{\text{DCDD}}}{2u_{\text{ref}}} \, \frac{\| \boldsymbol{\nabla} \|\mathbf{u}^h\| \| \, h_{\text{DCDD}}}{u_{\text{ref}}} \, , \tag{20}$$

where

$$h_{\text{DCDD}} = h_{\text{RGN}} \, . \tag{21}$$

Here u_{ref} is a reference velocity (such as $\|\mathbf{u}^h\|$ at the inflow, or the difference between the estimated maximum and minimum values of $\|\mathbf{u}^h\|$). Combining Eqs. (19) and (20), we obtain

$$\nu_{\text{DCDD}} = \frac{1}{2} \left(\frac{\|\mathbf{u}^h\|}{u_{\text{ref}}} \right)^2 (h_{\text{DCDD}})^2 \, \| \, \boldsymbol{\nabla} \|\mathbf{u}^h\| \, \| \, . \tag{22}$$

Then the DCDD stabilization is defined as

$$S_{\text{DCDD}} = \sum_{e=1}^{n_{el}} \int_{\Omega^e} \rho \boldsymbol{\nabla} \mathbf{w}^h : \left([\nu_{\text{DCDD}} \mathbf{r}\mathbf{r} - \boldsymbol{\kappa}_{\text{CORR}}] \cdot \boldsymbol{\nabla} \mathbf{u}^h \right) d\Omega \, , \tag{23}$$

where $\boldsymbol{\kappa}_{\text{CORR}}$ is defined as

$$\boldsymbol{\kappa}_{\text{CORR}} = \nu_{\text{DCDD}} (\mathbf{r} \cdot \mathbf{s})^2 \mathbf{s}\mathbf{s} \, . \tag{24}$$

6 LES MODEL

In the LES model we use in our computations, the subgrid viscosity based on the Smagorinsky model is defined as follows:

$$\nu_{\text{SMAG}} = (l_{\text{SMAG}})^2 \ (2\ \boldsymbol{\varepsilon}(\mathbf{u}^h) : \boldsymbol{\varepsilon}(\mathbf{u}^h))^{\frac{1}{2}} \ . \tag{25}$$

Here l_{SMAG} is the Smagorinsky length scale defined as

$$l_{\text{SMAG}} = (C_{\text{SMAG}}\ \Delta_{\text{SMAG}}) \ , \tag{26}$$

where C_{SMAG} ranges between 0.1 and 0.17, and Δ_{SMAG} is the grid filter width given as

$$\Delta_{\text{SMAG}} = 2\ (\Delta x\ \Delta y\ \Delta z)^{\frac{1}{3}} \ . \tag{27}$$

To take into account the near-wall effects, the Smagorinsky length scale is modified by using a Van Driest damping function as follows:

$$l_{\text{SMAG}} = (C_{\text{SMAG}}\ \Delta_{\text{SMAG}}) \left[1 - \mathrm{e}^{\left(\frac{y^+}{A^+}\right)}\right] \ , \tag{28}$$

where A^+ is a constant set to 26, and

$$y^+ = \frac{y u_\tau}{\nu} \ . \tag{29}$$

Here u_τ is the friction velocity:

$$u_\tau = \left(\frac{\tau_w}{\rho}\right)^{\frac{1}{2}} \ , \tag{30}$$

where τ_w is the wall shear stress.

7 TEST COMPUTATIONS

7.1 Introductory remarks

As test cases, we consider two problems: 3D plane channel flow at $Re_\tau = 395$ and an axial compressor rotor of non-free vortex (NFV) design. The first test case is used for evaluating the log-layer prediction of non-isotropic models. The DNS data provided in [29] is used as benchmark data. The second case is a highly loaded axial rotor designed using a NFV concept, with a power function ideal total head rise distribution along the radius. The spanwise gradient in blade loading results in characteristic 3D secondary flow filling the dominant rotor blade passage flow region. This NFV flow manifests itself in the torsion of interblade stream surface segments, modifies the flow turning, and influences the formation of endwall boundary layers in a complex manner shown in [30, 31].

7.2 Plane channel flow at $Re_\tau = 395$

This fully developed plane channel flow involves a unidirectional flow configuration characterized by a friction Reynolds number of $Re_\tau = u_\tau \delta/\nu = 395$, where δ is the half channel width. The direct numerical simulation (DNS) of this problem reported in [29] is regarded as highly accurate due to the very fine discretization used. Here we use that as benchmark data. The problem geometry is shown in Figure 1. The inflow

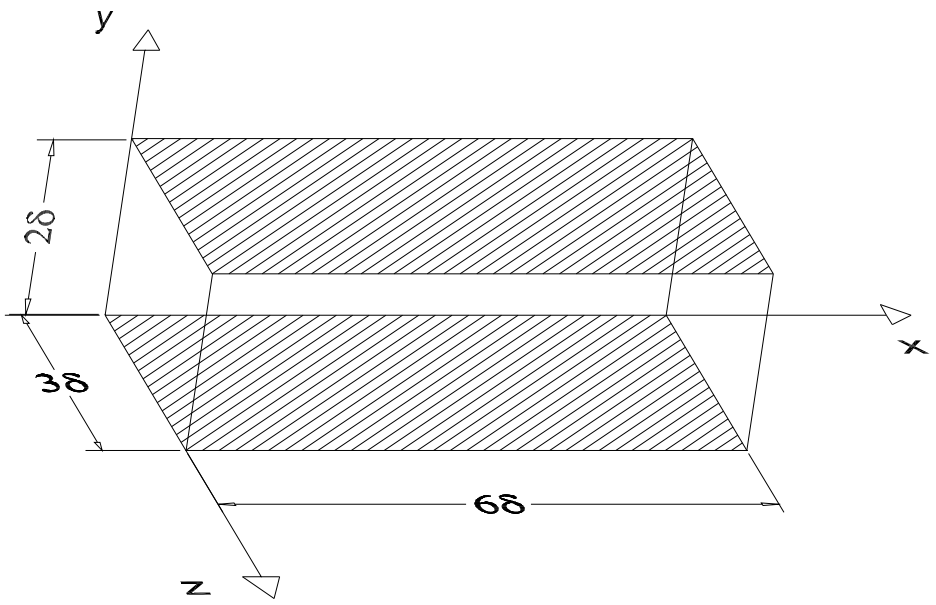

Figure 1: Plane channel flow at $Re_\tau = 395$. Problem geometry.

boundary conditions are extracted from a developed flow field computed with a RANS model, plus fluctuations in the form of a Gauss random distribution function in time. No-slip conditions are imposed on the walls, and the periodicity conditions at the lateral boundaries normal to the z axis.

The domain is discretized with a structured grid consisting of $120 \times 56 \times 56$ Q1Q1 elements. The grid is more refined near the walls (in the y direction) and also near the lateral boundaries normal to the z axis. The grid is uniform in the x direction. At the wall $\Delta y^+ = 1.8$, while $\Delta x^+ = 65$ and $\Delta z^+ = 21$. In the direction normal to the wall the first four nodes are in the region $y^+ \leq 10$. The CFL number is 0.5. In the LES computation, we set $C_{\text{SMAG}} = 0.15$. The problem is computed for 900 time steps to develop into a fully turbulent flow, and then an additional 6600 time steps to gather statistics.

Figure 2 shows the the axial velocity profiles obtained with the DNS simulation, LES

model, and DCDD stabilization. Figures 3, 4 and 5 show the Reynolds stress components

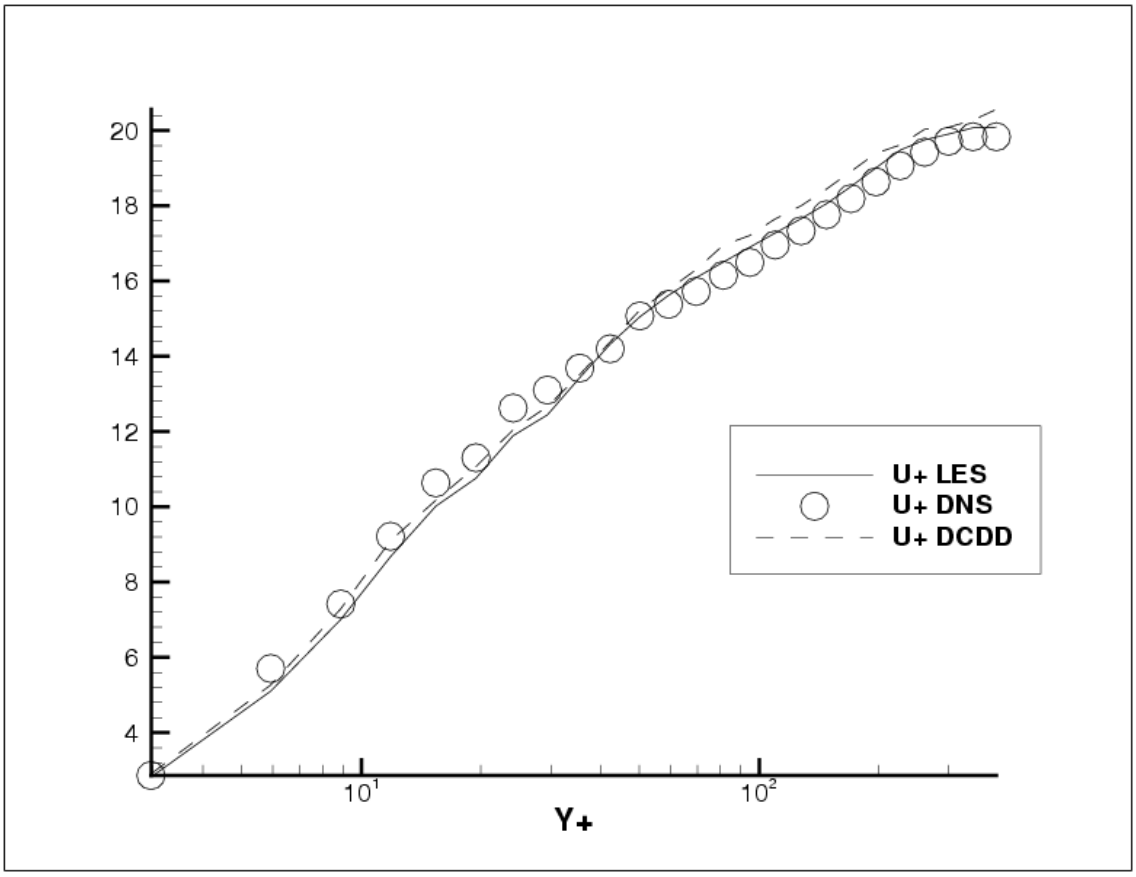

Figure 2: Plane channel flow at $Re_\tau = 395$. Axial velocity.

uu^+ ($=uu/u_\tau^2$), vv^+ ($=vv/v_\tau^2$), and ww^+ ($=ww/w_\tau^2$), obtained the DNS simulation, LES model, and DCDD stabilization. We observe from Figure 3 that in the LES and DCCD computations the uu^+ profile is predicted well within the viscous sub-layer region up to the log-layer region. We also observe that the LES model and DCCD stabilization overpredict the DNS stress in regions approaching the channel centerline. For the Reynolds stress component vv^+, which is critical in transitional flows, we see in Figure 4 that the results obtained with the DNS simulation, LES model, and DCDD stabilization compare well. For the Reynolds stress component ww^+, Figure 5 shows that there is a good general agreement between the results obtained with the DNS simulation, LES model, and DCDD stabilization.

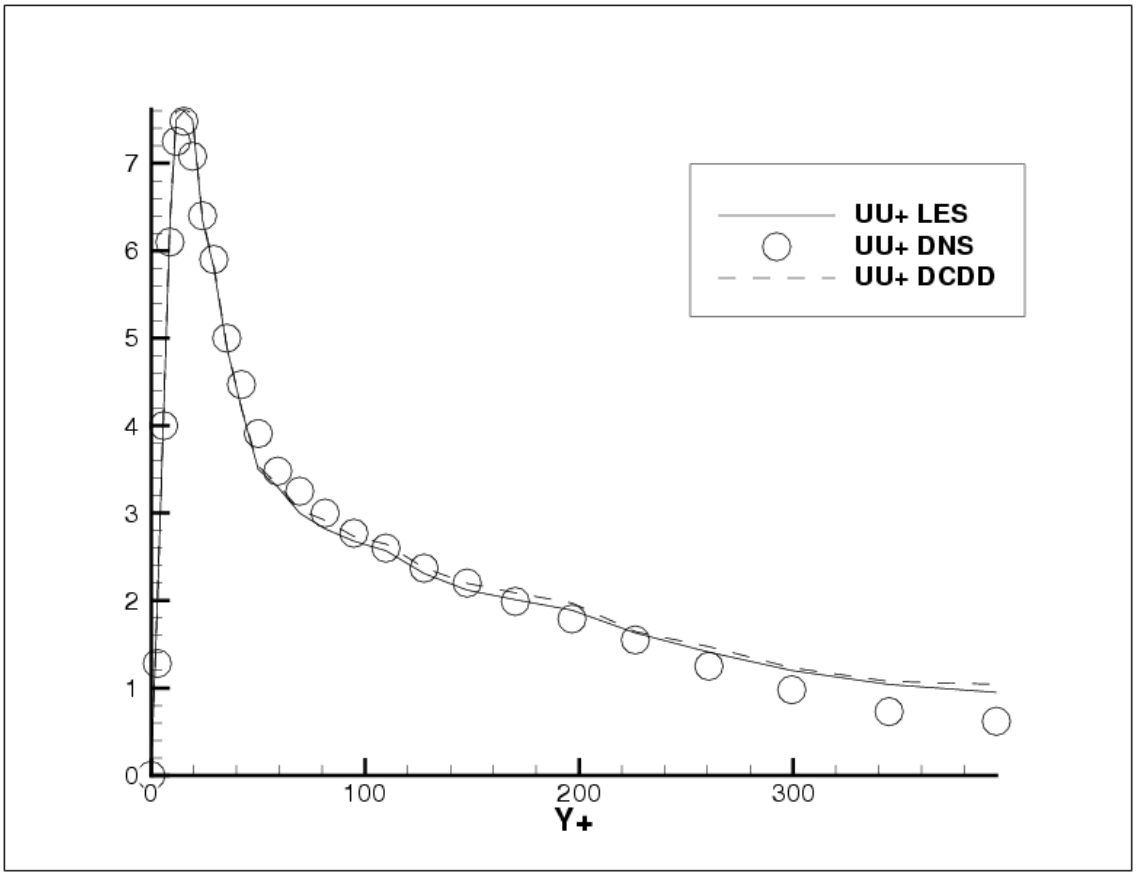

Figure 3: Plane channel flow at $Re_\tau = 395$. Reynolds stress component uu^+.

7.3 NFV axial flow rotor

The axial rotor consists of 12 unswept cambered plate blades with maximum blade thickness of 2 mm. The blades have a constant chord of 171 mm. The hub-to-tip diameter ratio is 0.676 and the blade solidity at mid-span is 1.23. The average chord-wise tip clearance is 3 mm. Figure 6 shows the blade configuration and provides more geometrical data.

The simulation is carried out at flow rate $\Phi = 0.5$ and Reynolds number 4×10^5 (based on the chord length and inflow speed at midspan). The thin blade profile permits the use of H-grid topology for the discretization of the computational domain, which is limited to the rotor blade passage and excludes the clearance region over the blade tip. We use a non-orthogonal body fitted grid with $180 \times 60 \times 40$ nodes (in the axial, pitchwise and spanwise directions). An adequate mesh refinement is used near the blade walls (with $y^+ = 2$ in the direction normal to the wall) and the hub and tip walls (with $y^+ \leq 10$). The CFL number is 0.5. In the LES computation, we set $C_{\text{SMAG}} = 0.15$. The inflow boundary conditions for the relative velocity components are obtained from the LDA

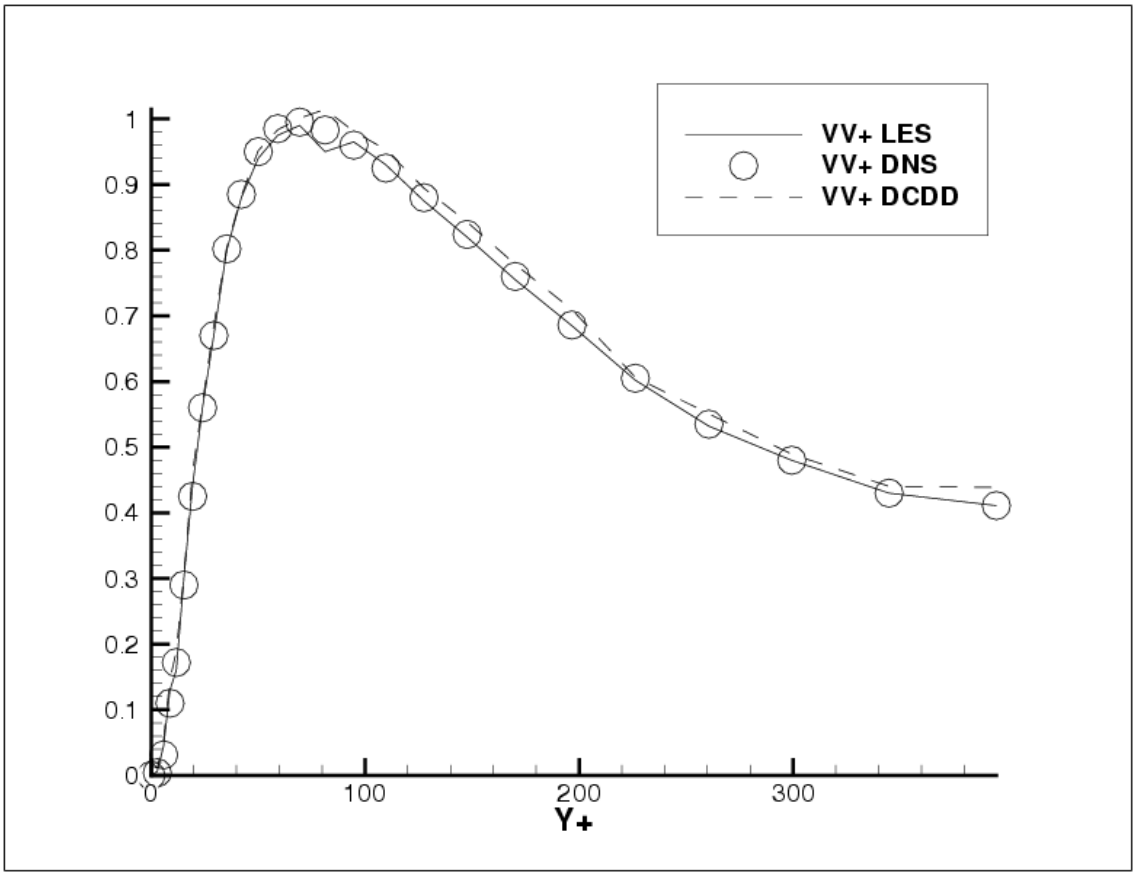

Figure 4: Plane channel flow at $Re_\tau = 395$. Reynolds stress component vv^+.

upstream measurements [30]. A fluctuating velocity field is superimposed to the average velocity as a Gauss random function distribution, with an average magnitude determined based on turbulence intensity measurements [32]. We impose flow periodicity conditions in the circumferential direction, and Neumann boundary conditions at the outflow.

Comparisons are based on examining the pitchwise flow structure. This is done in terms of the axial and radial flow coefficients, ϕ_{3a} $(= u_{3a}/U_c)$ and ϕ_{3r} $(= u_{3r}/U_c)$, and the ideal total head rise coefficient, ϕ_3 $(= 2Ru_{3p}/U_c$ for zero inlet swirl). Here, R is the tip radius, U_c is the maximum circumferential velocity, and u_{3a}, u_{3r}, and u_{3p} are the axial, radial, and circumferential absolute velocity components behind the rotor in the section (3) shown in Figure 6. Figures 7, 8, and 9 show, for LDA measurements, LES model and DCDD stabilization, the axial flow coefficient, ideal total head rise coefficient, and radial flow coefficient.

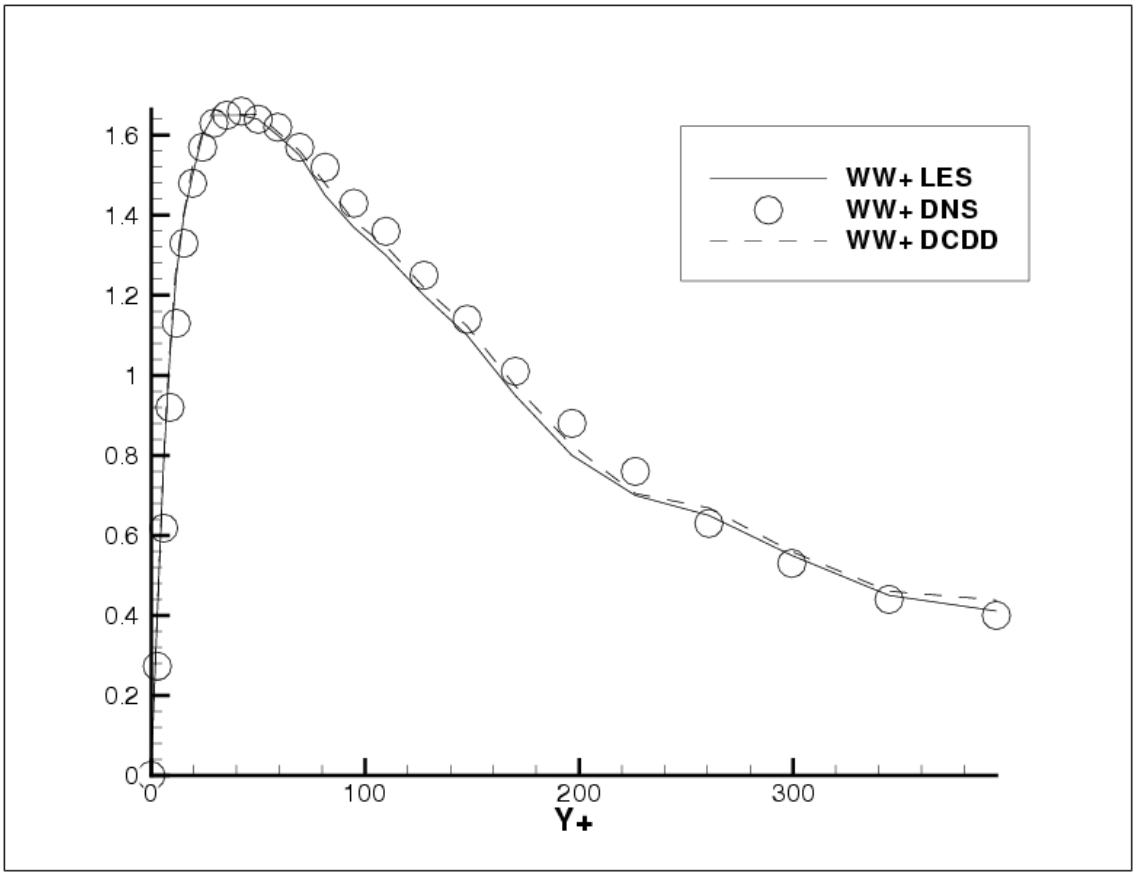

Figure 5: Plane channel flow at $Re_\tau = 395$. Reynolds stress component ww^+.

8 CONCLUDING REMARKS

We provided an overview of the Streamline-Upwind/Petrov-Galerkin (SUPG) and Pressure-Stabilizing/Petrov-Galerkin (PSPG) formulation, calculation of the stabilization parameters involved, and the Discontinuity Capturing Directional Dissipation (DCDD). The DCDD stabilization was first introduced as a complement to the SUPG and PSPG stabilizations for the computation of incompressible flows in the presence of sharp solution gradients. The DCDD stabilization takes effect where there is a sharp gradient in the velocity field and introduces dissipation in the direction of that gradient. The length scale used in defining the DCDD stabilization is based on the solution gradient. We call that the diffusive length scale. The way the DCDD stabilization is added to the finite element formulation precludes augmentation of the SUPG effect by the DCDD effect when the advection and discontinuity directions coincide. We described how the DCDD stabilization, in combination with the SUPG and PSPG stabilizations, can be applied to the computation of turbulent flows. With two test computations, we compared the results obtained with the DCDD stabilization with those obtained with an LES turbulence model.

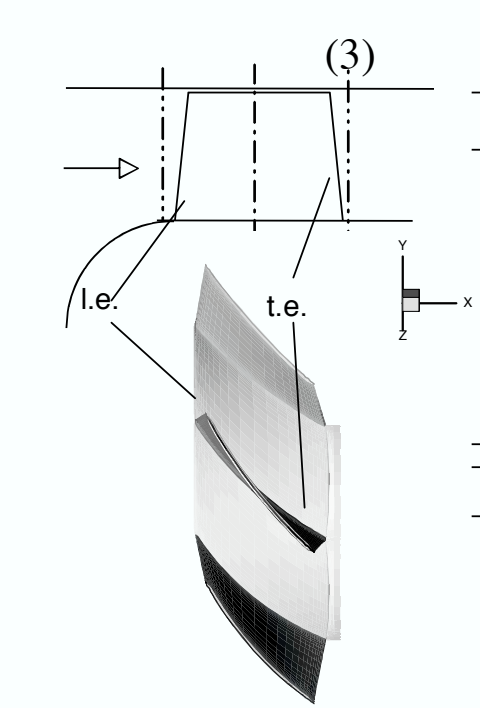

USW BUP29 rotor	
blade nr	12
hub-to-tip diameter ratio	0.676
χ %span	2.5
Φ_D	0.5
Ψ_D	0.7

	hub	midspan	tip
solidity	1.53	1.24	1.05
stagger angle, deg	47.9	42.2	38.3
camber angle, deg	27.4	23.1	19.9

Figure 6: NFV axial flow rotor. Blade geometry.

The comparisons show that the DCDD stabilization has a good potential for playing a significant role in computation of turbulent flows.

ACKNOWLEDGMENTS

This work was supported by the US Army Natick Soldier Center and NASA JSC. We thank Professor Alessandro Corsini for his valuable comments.

REFERENCES

[1] P. Sagaut, *Large eddy simulation for incompressible flows – An introduction*. Springer-Verlag, New York, 1998.

[2] T. Dubois, F. Jauberteau, and R. Temam, "Solution of the incompressible navier-stokes equations by the nonlinear galerkin method", *Journal of Scientific Computing*, **8** (1993) 167–194.

[3] T.J.R. Hughes, "Multiscale phenomena: Green's functions, the Dirichlet-to-Neumann formulation, subgrid scale models, bubbles, and the origins of stabilized methods", *Computer Methods in Applied Mechanics and Engineering*, **127** (1995) 387–401.

[4] T.J.R. Hughes, L. Mazzei, and K.E. Jansen, "Large eddy simulation and the variational multiscale method", *Computing and Visualization in Science*, **3** (2000) 47–59.

[5] T.J.R. Hughes, L. Mazzei, A.A. Oberai, and A. Wray, "The multiscale formulation of large eddy simulation: Decay of homogeneous isotropic turbulence", *Physics of Fluids*, **13** (2001) 505–512.

[6] K.E. Jansen, "A stabilized finite element method for computing turbulence", *Computer Methods in Applied Mechanics and Engineering*, **174** (1999) 299–317.

[7] T.J.R. Hughes and A.N. Brooks, "A multi-dimensional upwind scheme with no crosswind diffusion", in T.J.R. Hughes, editor, *Finite Element Methods for Convection Dominated Flows*, AMD-Vol.34, 19–35, ASME, New York, 1979.

[8] A.N. Brooks and T.J.R. Hughes, "Streamline upwind/Petrov-Galerkin formulations for convection dominated flows with particular emphasis on the incompressible Navier-Stokes equations", *Computer Methods in Applied Mechanics and Engineering*, **32** (1982) 199–259.

[9] T.E. Tezduyar and T.J.R. Hughes, "Development of time-accurate finite element techniques for first-order hyperbolic systems with particular emphasis on the compressible Euler equations", NASA Technical Report NASA-CR-204772, NASA, 1982, http://ntrs.nasa.gov/archive/nasa/casi.ntrs.nasa.gov/19970023187_1997034954.pdf.

[10] T.E. Tezduyar and T.J.R. Hughes, "Finite element formulations for convection dominated flows with particular emphasis on the compressible Euler equations", in *Proceedings of AIAA 21st Aerospace Sciences Meeting*, AIAA Paper 83-0125, Reno, Nevada, (1983).

[11] T.J.R Hughes and T.E. Tezduyar, "Finite element methods for first-order hyperbolic systems with particular emphasis on the compressible Euler equations", *Computer Methods in Applied Mechanics and Engineering*, **45** (1984) 217–284.

[12] T.E. Tezduyar, "Stabilized finite element formulations for incompressible flow computations", *Advances in Applied Mechanics*, **28** (1992) 1–44.

[13] T.E. Tezduyar and Y.J. Park, "Discontinuity capturing finite element formulations for nonlinear convection-diffusion-reaction equations", *Computer Methods in Applied Mechanics and Engineering*, **59** (1986) 307–325.

[14] T.J.R. Hughes, L.P. Franca, and M. Balestra, "A new finite element formulation for computational fluid dynamics: V. Circumventing the Babuška–Brezzi condition: A stable Petrov–Galerkin formulation of the Stokes problem accommodating equal-order interpolations", *Computer Methods in Applied Mechanics and Engineering*, **59** (1986) 85–99.

[15] T.E. Tezduyar and Y. Osawa, "Finite element stabilization parameters computed from element matrices and vectors", *Computer Methods in Applied Mechanics and Engineering*, **190** (2000) 411–430.

[16] T.E. Tezduyar, "Adaptive determination of the finite element stabilization parameters", in *Proceedings of the ECCOMAS Computational Fluid Dynamics Conference 2001 (CD-ROM)*, Swansea, Wales, United Kingdom, (2001).

[17] T.E. Tezduyar, "Stabilized finite element formulations and interface-tracking and interface-capturing techniques for incompressible flows", in M.M. Hafez, editor, *Numerical Simulations of Incompressible Flows*, World Scientific, New Jersey, (2003) 221–239.

[18] T.E. Tezduyar, "Computation of moving boundaries and interfaces and stabilization parameters", *International Journal for Numerical Methods in Fluids*, **43** (2003) 555–575.

[19] T. Tezduyar, "Stabilization parameters and local length scales in SUPG and PSPG formulations", in *Proceedings of the Fifth World Congress on Computational Mechanics*, On-line publication: http://wccm.tuwien.ac.at/, Paper-ID: 81508, Vienna, Austria, (2002).

[20] T. Tezduyar and S. Sathe, "Stabilization parameters in SUPG and PSPG formulations", *Journal of Computational and Applied Mechanics*, **4** (2003) 71–88.

[21] T.E. Tezduyar, "Calculation of the stabilization parameters in SUPG and PSPG formulations", in *Proceedings of the First South-American Congress on Computational Mechanics (CD-ROM)*, Santa Fe–Parana, Argentina, (2002).

[22] T.E. Tezduyar, "Finite element methods for fluid dynamics with moving boundaries and interfaces", in E. Stein, R. De Borst, and T.J.R. Hughes, editors, *Encyclopedia*

of Computational Mechanics, Volume 3: Fluids, Chapter 17, John Wiley & Sons, 2004.

[23] T.E. Tezduyar, "Calculation of the stabilization parameters in finite element formulations of flow problems", in S.R. Idelsohn and V. Sonzogni, editors, *Applications of Computational Mechanics in Structures and Fluids*, 1–19, CIMNE, Barcelona, Spain, 2005.

[24] B.P. Leonard, "A stable and accurate convective modeling procedure based on quadratic upstream interpolation", *Computer Methods in Applied Mechanics and Engineering*, **19** (1979) 59–98.

[25] T. Kawamura and K. Kuwahara, "Computation of high reynolds number flow around a circular cylinder with surface roughness", in *AIAA 22nd Aerospace Sciences Meeting*, Reno, Nevada, (1984).

[26] B. Engquist, P. Lotstedt, and B. Sjogreen, "Nonlinear filter for efficient shock computation", *Mathematics of Computation*, **52** (1989) 509–536.

[27] D. Borello, P. Borrelli, E. Quagliata, and F. Rispoli, "A multi-grid additive and distributive parallel algorithm for finite element turbomachinery cfd", in *Proceedings of the ECCOMAS Computational Fluid Dynamics Conference 2001 (CD-ROM)*, Swansea, Wales, United Kingdom, (2001).

[28] D. Borello, A. Corsini, and F. Rispoli, "A finite element overlapping scheme for turbomachinery flows on parallel platforms", *Computers and Fluids*, **32/7** (2003) 1017–1047.

[29] R. Moser, J. Kim, and P. Moin, "Direct numerical simulation of turbulent channel flow up to $Re_\tau = 590$", *Physics of Fluid*, **11** (1999) 943–948.

[30] J. Vad and F. Bencze, "Three-dimensional flow in axial flow fans of non-free vortex design", *International Journal of Heat and Fluid Flow*, **19** (1998) 601–607.

[31] A. Corsini and F. Rispoli, "The role of forward sweep in subsonic axial fan rotor aerodynamics at design and off-design operating conditions", ASME Paper GT2003-38671, (2003).

[32] J. Vad. "Unpublished notes", 1999.

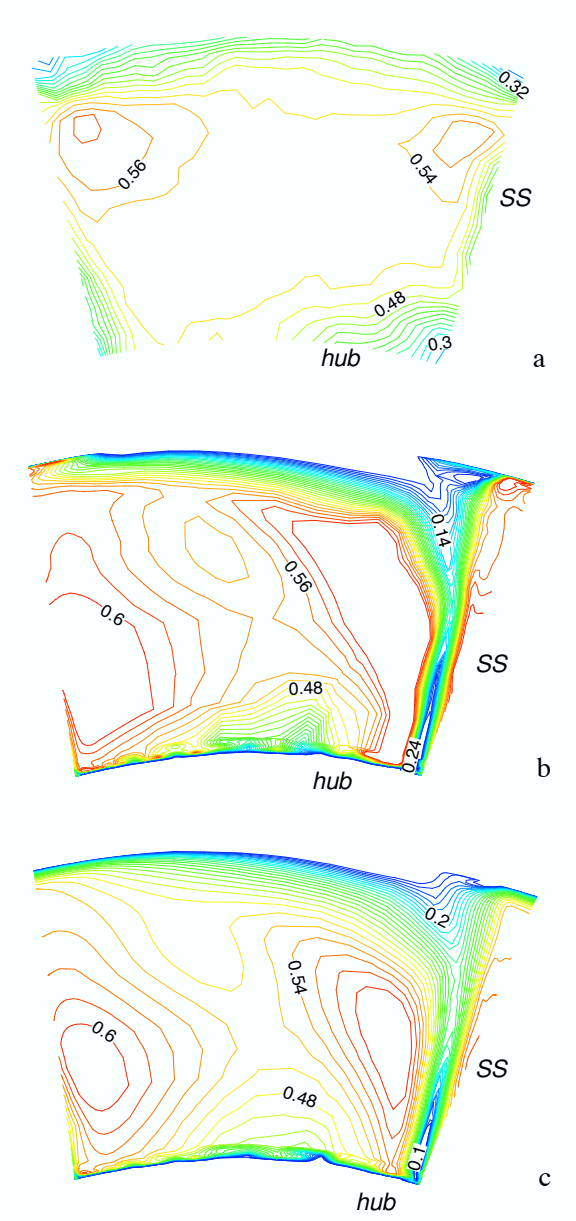

Figure 7: NFV axial flow rotor. Axial flow coefficient behind rotor: a) LDA, b) LES, c) DCDD.

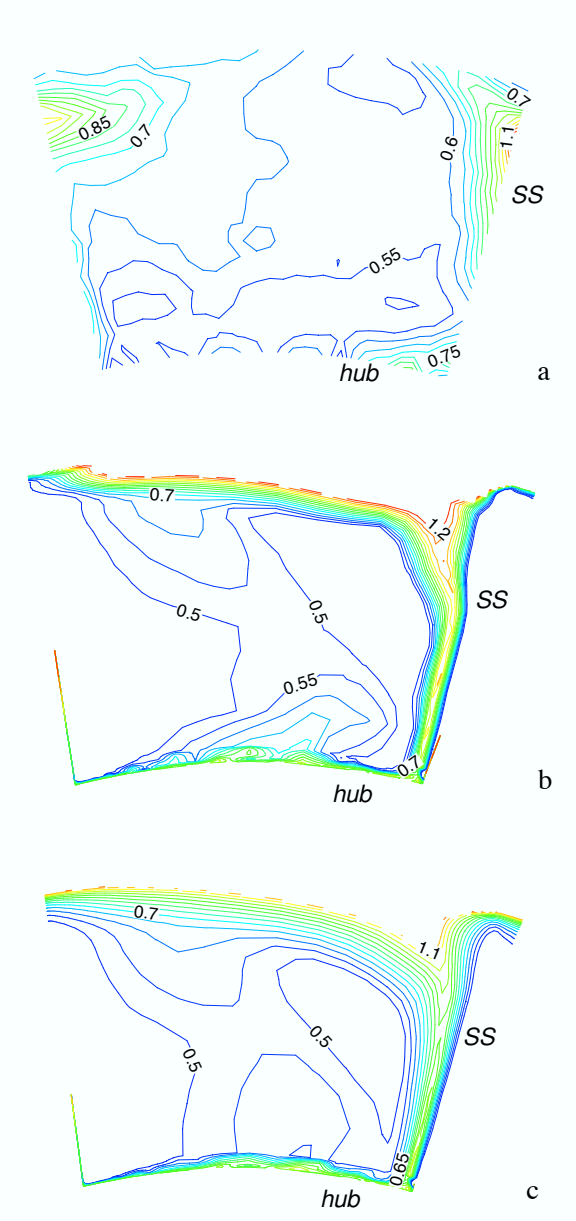

Figure 8: NFV axial flow rotor. Ideal total head rise coefficient behind rotor: a) LDA, b) LES, c) DCDD.

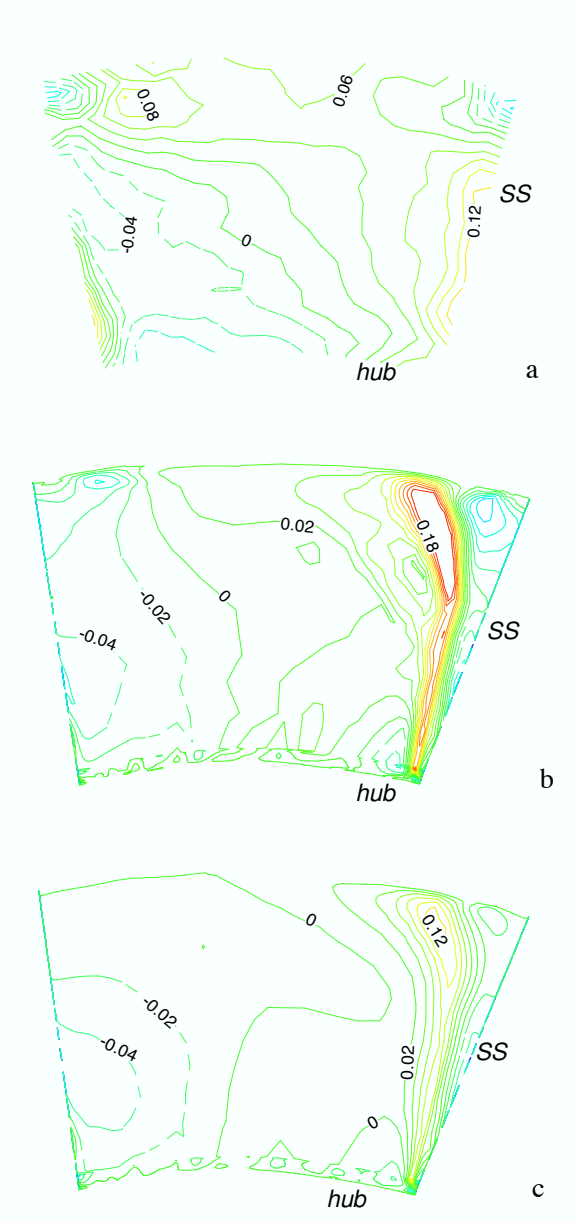

Figure 9: NFV axial flow rotor. Radial flow coefficient behind rotor: a) LDA, b) LES, c) DCDD.